Environmental Response in Coupled Energy and Water Cloud Impact Parameters Derived from A-Train Satellite, ERA-Interim and MERRA-2

Lu Sun[1,5], A.D. Rapp[2], T. L'Ecuyer[2,3], A.S. Daloz[2,3,4] and E. Nelson[2,6]

[1]Department of Atmospheric Sciences, Texas A&M University, College Station, TX, USA.

[2]Atmospheric and Oceanic Sciences Department, University of Wisconsin-Madison, Madison, WI, USA.

[3]Center for Climate Research, University of Wisconsin-Madison, Madison, WI, USA.

[4]CICERO, Gaustadalléen 21, Oslo, Norway.

[5]Department of Physics, University of Auckland, Auckland, New Zealand.

[6]Jet Propulsion Laboratory, California Institute of Technology, Pasadena, CA, USA

Corresponding author: Lu Sun (lusun@tamu.edu)

Key Points:

- Coupled cloud impact parameters in reanalyses and observations have similar patterns, but opposite biases in high and low cloud regimes
- Reanalyses show less (more) heating (cooling) of the atmosphere in high (low) sea surface temperature and column water vapor environments
- Water vapor is a stronger control than sea surface temperature on coupled cloud impact parameters, especially in reanalyses

Abstract

Understanding the connections between the latent heating from precipitation and atmospheric cloud radiative effects is essential for climate models to accurately represent the cross-scale links between cloud microphysics and global energy and water cycles. In this paper, two energy and water cycle coupling cloud impact parameters (CIPs), radiative cooling efficiencies, R_c, and heating efficiencies, R_h, are used to characterize how efficiently clouds can heat the atmosphere or cool the surface, respectively, per unit rain from A-Train observations and two reanalyses. Global distributions of CIPs are highly dependent on cloud regime and reanalyses fail to simulate strong R_c and R_h at high sea surface temperature (SST)/column water vapor (CWV) in deep convection regions like the Indo-Pacific warm pool, but produce stronger R_c and R_h over SST/CWV associated with shallow, warm rain systems as in the eastern Pacific marine stratocumulus regions. The dynamic regime controls the sign of R_h, while the CWV appears to be the larger control on the magnitude. The magnitude of R_c is highly coupled to the dynamic regime. Observations also show two thermodynamic regimes of strong R_c, at low SST and CWV and at high SST and CWV, only the former of which is captured by the reanalyses. While the reanalyses generate fairly similar climatologies in the frequency distributions of environmental states, differences in R_c and R_h between reanalyses and A-Train are linked to differences in the vertical profiles of the temperature, specific humidity and vertical velocity for precipitating cloud scenes.

Plain Language Summary

Accurate projection of future climate requires understanding coupled interactions between clouds, precipitation, and their environment. Here we use satellite observations to calculate two parameters to reveal how efficiently clouds can heat the atmosphere or cool the surface per unit rain and compare to those simulated by observationally-constrained reanalysis datasets. The reanalyses show similar global patterns but have weaker atmospheric heating and surface cooling per unit rain in areas of deep convection and opposite effects in low cloud regions. Examination of these parameters as a function of their environment shows that reanalyses cool the atmosphere too much per unit rain in environments with low sea surface temperatures and water vapor. In regions with high sea surface temperature and water vapor, deep convection in reanalyses does not heat the atmosphere enough per unit rain. Whether clouds occur in regions of large-scale ascent or descent determines whether clouds heat or cool the atmosphere and how strong the clouds cool the surface, while sea surface temperature and water vapor control the strength of the atmospheric heating. Both observations and reanalyses suggest that water vapor is the stronger control on how much clouds heat the atmosphere per unit rain.

1. Introduction

The role of clouds in climate feedback, which highly depends on cloud macro- and micro- physical properties, remains one of the largest uncertainties in current climate projection (Bony and Dufresne 2005; Randall et al. 2007; Dessler, 2010; Choi et al. 2014 Bony et al. 2015; Ceppi et al. 2017). The macro- and microphysical properties impact both cloud radiative effects and the precipitation intensity of the clouds (Mace et al. 2017; Wood et al. 2012). To predict cloud feedbacks accurately in the climate system, two elements should be further understood: the ability of climate models and physical parameterizations to produce cloud and precipitation from changing atmospheric states and the ability to use these cloud properties to estimate the radiative energy fluxes that, in turn, heat the atmosphere or cool the surface (Xu et al. 2005; 2016).

Thus, cloud radiative effects and cloud feedback are highly connected to the precipitation process and the efficiencies in converting cloud condensate to surface precipitation (Stevens and Bony 2013; Bony et al. 2015). These links between the water and energy cycles occur across a variety of spatial and temporal scales. At global annual mean timescales, energy constrains precipitation, with precipitation increases primarily constrained by atmospheric radiative cooling (Held and Soden 2006; Stephens and Ellis 2008; O'Gorman, P.A. et al. 2012; Pendergrass and Hartmann 2014; Dinh and Fueglistaler 2017). Because the cloud radiative influence on the exchange of radiative fluxes between the atmosphere and surface are intimately linked with the water cycle through radiative-convective equilibrium, the strength and location of cloud radiative effects and precipitation intensity is not independent and their relative magnitudes in global models depend strongly on the way clouds and convection are parameterized. The coupling of radiation-precipitation occurs across scales ranging from those of climatic scale (Allan et al. 2009; Previdi et al. 2010; Andrew et al. 2010, O'Gorman, P.A. et al. 2012), El Niño and Southern Oscillation (ENSO) (L'Ecuyer et al. 2006), Madden-Julian Oscillation (MJO) (Kim et al. 2015) to mesoscale convective system (MCSs) (Bouniol et al. 2016). This multiscale coupling should be accurately represented for models to simulate atmospheric radiative heating and cooling successfully. Failing to simulate the coupling of radiation-precipitation relationships at each spatial and temporal scale yields large uncertainties in representing cloud cover, precipitation (both stratiform precipitation and convective precipitation) and thermodynamic forcing. (Wilcox et al. 2001; O'Brien et al. 2013; Betts et al. 2014; Calisto et al. 2014). The phase of ENSO and MJO coupling with large-scale global circulation may also be misrepresented and lead to large bias in climate models and reanalysis if the radiation-precipitation coupling relationship is not well represented (L'Ecuyer et al. 2006, Kim et al. 2015).

The way that clouds and precipitation are currently parameterized and coupled in General Circulation Models (GCMs) is known to produce errors in radiative and latent heating distributions, such as insufficient low cloud cover in subtropical subsidence regions (Kay et al. 2012), warm sea surface temperature (SST) biases in the southeast Pacific (Yu and Mechoso 1999; Dai et al. 2003; Li et al. 2004), the presence of a ubiquitous tropical rain band south of the equator (Waliser et al. 2003; Masunaga and L'Ecuyer 2011), premature onset of deep convection particularly over land (Dai and Trenberth 2004; Grabowski et al. 2006; Clark et al. 2007), the lack of Madden-Julian Oscillation (MJO) (Lee et al. 2001), and underestimates of the Walker circulation response to El Nino (L'Ecuyer and Stephens, 2007; Kociuba and Power 2015). The role of the coupling cloud–radiation interaction also affects the simulation of the MJO (Kim et al. 2013) and can amplify the warm El Nino phases of the El Nino-Southern Oscillation (ENSO) (Radel et al. 2016).

In addition to cloud-precipitation-radiation biases in climate models, reanalyses are also biased with respect to the observations, mainly due to the different assimilation methods and forecasting systems they use, even though reanalyses are constrained by observations. Clouds, radiation, and precipitation represented in reanalyses generally agree with observations at the global mean scale, however, large biases occur at the regional scale. Dolinar et al. (2016) compared five reanalysis precipitation rates (PRs) with those from the Tropical Rainfall Measurement Mission (TRMM) and found reanalysis PRs overestimate the large-scale TRMM mean by 3% - 20 %, and also overestimate PRs in both ascent and subsidence regimes. PR biases over the ascent regime are an order of magnitude larger than those over the descent regime. Also, the biases in reanalysis caused by a lack of mid-level and/or low clouds, water vapor, anomalous temperature structures and overestimated atmospheric stability represented by stronger subsidence result in both radiative and precipitation biases (Naud et al. 2014; Griggs et al. 2008; Liu et al. 2016; Stengel et al. 2018). Both reanalysis and some climate models may have cloud, convection, or boundary layer scheme problems that lead to a large bias in individual weather systems and an inability to simulate the correct surface solar radiation (Naud et al. 2014), as well as global precipitation (Bodas-Salcedo et al. 2007). Approximations used in the model's representation of moist processes strongly affect the quality and consistency of both cloud radiative effect (CRE) and the hydrological cycle (Dee et al. 2011; Bosilovich et al. 2017).

In some numerical models, such as the minimal model of a moist equatorial atmosphere of Fuchs and Raymond (2001), the coupled ocean-atmosphere model of Bretherton and Sobel (2002) and Sobel and Gildor (2003), they fixed the relationship between CRE and precipitation in radiative heating and cooling parameterization processes, assuming that clouds reduce the clear-sky radiative cooling by an amount proportional to precipitation. This cloud-radiation feedback parameter was determined by the Tropical Ocean Global Atmosphere Coupled Ocean-Atmosphere Response Experiment (TOGA COARE) radiation dataset and fixed at 0.2, but they note that the uncertainties are as large as 50%.

Emerging state-of-the-art satellite observations offer the opportunity to examine this relationship in detail. In this context, L'Ecuyer et al. (2006) and Daloz et al. (2018) explored five monthly mean cloud impact parameters (CIPs) based on both TRMM and A-Train satellite observations that can connect the precipitation and cloud radiative effects to represent the cloud processes in climate models better. There are two energy and water cycle coupling parameters in the definition of CIPs, the surface cooling efficiency, R_c and atmospheric heating efficiency, R_h, representing how efficiently a precipitating cloud can cool the surface or heat the atmosphere, respectively, per unit latent heat release from rainfall. These observational radiative efficiencies were first used to show the evidence of cloud feedback pathways associated with ENSO in the Pacific by L'Ecuyer et al. (2006). They demonstrated that clouds in the East Pacific heat the atmosphere more efficiently and cool the surface less efficiently per unit rainfall with increasing SST, suggesting that changes in cloud characteristics may reinforce changes in the Walker circulation during El Niño events. Their estimates of R_c range from -0.7 to 0 and -0.1 to 0.4 for R_h at the monthly scale, which is considerably different from the constant of 0.2 used in the aforementioned modeling studies with biases greater than 100%. In Daloz et al. (2018), they used A-Train observations and reanalyses to demonstrate the global distribution and climatology of CIPs for the first time. The global mean spatial distributions of CIPs were compared comprehensively, and while they briefly examined the relationship between CIPs and monthly mean vertical pressure velocity at 500hpa (ω_{500}), there was little discussion on the relationship to the thermodynamic environments or the variations in the strength off the coupling at different time scales. As the cloud radiative feedback on atmospheric circulation is still one of the most important topics in climate studies, the environmental impacts on CIPs should be studied in more detail to help improve the performance of GCM and reanalysis (Bretherton et al. 2002, Bretherton et al. 2005; Muller et al. 2012; Bony et al. 2015). Also, the high sensitivity of the strength of the cloud-radiation feedbacks in the current models indicate that investigation of the ratio between CRE and precipitation in observation can provide a reference for model designers (Ying et al. 2016).

One of the key obstacles to accurately understanding the feedback processes of clouds in climate is their dependence on the environments in which the clouds reside (Stephens 2005). Studies show that different cloud regimes, which determine the sign and strength of coupled

CIPs (discussed more later), are associated with both dynamical and thermodynamical environmental variables, such as SST (Xu et al. 2009, Eitzen et al. 2010), CWV and ω_{500}. Correspondingly, they also influence the coupling between precipitation and radiation (Wang and Sobel 2011). Kubar et al. (2012) reported a strong correlation between low topped cloud fractions and SST and ω_{500}. They also found that the correlation increased with increasing averaging time scales (Kubar et al 2012). Their findings indicate that when environmental variables change, such as SST and ω anomalies during an ENSO event, the fraction of clouds should change, leading to a corresponding change of cloud radiative forcing, which may strengthen or dampen large-scale circulation and impact precipitation intensity. This suggests further study of the coupling CRE and precipitation with the environment is needed. In addition, the coupling of CRE and precipitation is needed in environmental control experiments (Larson et al. 1999) because both CRE and precipitation are susceptible to changes in SST and water vapor (Larson et al. 1999, 2003a, 2003b). However, in modeling experiments, they are often tested separately instead of coupled. Additionally, radiative heating/cooling and precipitation are constrained under radiative-convective equilibrium (RCE). Studies show that under RCE assumption, temperature and water vapor have positive feedback in atmospheric longwave cooling (Allan 2009; Allan 2011; Pendergrass and Hartmann 2014; Colman, 2015), but L'Ecuyer et al. (2006) demonstrated that RCE cannot be met locally due to the highly variable nature of frequency, structure, and radiative properties of clouds and precipitation, which also motivates further examination of the dependence of coupled CIPs on the environment.

Overall, the main goal of this study is to evaluate the range of energy and water cycle coupling CIPs in both A-Train satellite and reanalysis datasets and to understand how they are linked to the dynamic and thermodynamic environment. A comparison in the global distribution of A-Train-derived and reanalysis-derived coupling CIPs at different time scales is first conducted. Given the aforementioned important links between the environment and precipitation, radiation and their coupling, the analysis of Daloz et al. (2018) is expanded to also include not only the CIP relationship with ω_{500}, but also SST and CWV. Observational and reanalysis coupling CIPs are conditionally sampled by matched environmental variables to determine how well reanalyses capture interactions among radiation-precipitation coupling, thermodynamic environments, and the corresponding large circulation. Profiles of humidity, air temperature and vertical velocity profiles are then analyzed to reveal how reanalysis differences in environmental states are linked to coupled CIP differences from the observations.

2. Data and Methodology

2.1 Satellite observations

The coupled CIPs are calculated from standard CloudSat-CALIPSO data products, including 2B-FLXHR-LIDAR (Stephens et al. 2002 and 2008; L'Ecuyer et al. 2008), 2B-GEOPROF-LIDAR (Stephens et al. 2002, 2008 and 2017; Sassen et al. 2008; Mace et al. 2009) and 2C-RAIN-PROFILE (Lebsock and L'Ecuyer 2011), and the Advanced Microwave Scanning Radiometer–Earth Observing System (AMSR-E) rainfall product, AE_RAIN (Wilheit 2003; Kummerow et al. 2010). CloudSat is a polar-orbiting satellite with a 98° orbital inclination carrying a 94 GHz (W-band) Cloud Profiling Radar (CPR), which is used to probe the vertical structure of clouds and precipitation (Stephens et al. 2008; Stephens et al. 2017; L'Ecuyer and Jiang 2010; Mace et al. 2014). CALIPSO uses the cloud-aerosol lidar with orthogonal polarization (CALIOP) to probe the vertical structure and properties of thin clouds and aerosols. With the combination of both CPR and CALIOP, there is an improved ability to detect thin cirrus and low clouds, especially when multiple layered clouds exist. The 2B-GEOPROF-LIDAR dataset provides the cloud layer and cloud top information to distinguish the heights and the number of cloud layers. The precipitation is provided by the 2C-RAIN-PROFILE dataset, which uses the two-way path integrated attenuation (PIA) of the entire atmospheric column to determine the presence of precipitation within the column (Haynes et al. 2007; Haynes et al. 2009; Stephens et al. 2008; Lebsock et al. 2011). However, the CPR has limitations in detecting heavy rain because of attenuation (Behrangi et al, 2012). To mitigate this limitation, rain rate derived from AMSR-E observations is used whenever the AMSR-E rain rate exceeds 2C-RAIN-PROFILE. AMSR-E is a total power passive-microwave (MW) radiometer system on aboard NASA EOS Aqua satellite with twelve channels and six frequencies measuring brightness temperature at 6.925, 10.65, 18.7, 23.8, 36.5 and 89.0GHz. Rain rate and rain type over ocean are from the AE_RAIN products generated via the Goddard Space Flight Center (GSFC) Profiling algorithm (GPROF2010) (Wilheit 2003; Kummerow et al. 2010; Kummerow et al. 2015). This study uses an existing rainfall subset that collocated AMSR-E rainfall products with the CloudSat track (Global Hydrology Resource Center/MSFC/NASA, 2009). One thing to note is that currently the CloudSat 2C-RAIN-PROFILE dataset is only applied over ocean (Lebsock et al 2011), so the coupled CIPs are only calculated over the ocean.

Radiative fluxes are used in the calculation of coupled CIPs and are provided by 2B-FLXHR-LIDAR (Stephens et al. 2008; L'Ecuyer et al. 2011), referred to hereafter as 2BFLX. 2BFLX blends information from the A-Train constellation including CloudSat's CPR, the CALIPSO satellite's CALIOP, and the Moderate Resolution Imaging Spectroradiometer (MODIS) and AMSR-E instruments on the Aqua satellite to generate vertically-resolved profiles of broadband radiation using a radiative transfer model (L'Ecuyer et al. 2008; Henderson et al. 2013). The 2BFLX algorithm, with the combination of multisensor observations, brings a more accurate and comprehensive perspective in determining the radiative impacts of clouds and aerosols.

2.2 Reanalyses

This study compares the coupled CIPs from two modern reanalyses, MERRA-2 and ERA-Interim with A-Train derived products from September 2006 – December 2010 for 60°S - 60°N. The relationship between the environment and coupled CIPs is also evaluated.

2.2.1 MERRA-2

MERRA-2 (Gelaro et al. 2017; Bosilovich et al. 2015b; Bosilovich et al. 2016; Bosilovich et al. 2017) replaces the previous MERRA with increased resolution, improvements in the GEOS-5 model, and in the assimilation system. The new system enables assimilation of modern hyperspectral radiance and microwave observations as well as GPS-Radio Occultation datasets, and is the first long-term reanalysis that assimilates space-based observations of aerosol. After 2005, ozone observations are included. Several upgrades have been made to the physical parameterization schemes including an increase in reevaporation of frozen precipitation and cloud condensate (Molod et al. 2015). The new reanalysis dataset now contains a Tokioka-type trigger (Bacmeister and Stephens, 2011) on deep convection as part of the relaxed Arakawa-Schubert convective parameterization (Moorthi and Suárez 1992; Cullather et al. 2014). In our studies, we use tavg1_2d_rad_Nx 1-hourly time-averaged data to calculate the radiative fluxes at surface and atmosphere and total precipitation from tav1_2d_flx_Nx 1-hourly time-averaged data to calculate the latent heating.

2.2.2 ERA-Interim

ERA-Interim (Dee et al. 2011) is a global atmospheric reanalysis beginning in 1979, developed by the European Center for Medium Range Forecasts (ECMWF). ERA-Interim replaced the previous reanalysis dataset from the ECMWF, ERA-40. Between ERA-40 and ERA-Interim, changes to the convective and boundary layer cloud schemes were made. For example, the convective cloud scheme can now be triggered at night, which increases its atmospheric stability and therefore creates less precipitation (Dee et al. 2011). The new moist boundary layer scheme reduces the underestimate of stratocumulus clouds because of changes in the inversion strength and height (Kohler et al. 2011). Convection, vertical motion, radiative heating and turbulence are connected to cloud generation via the prognostic cloud scheme (Jakob 1998). The Rapid Radiative Transfer Model computes radiation (Mlawer et al. 1997). In this study, we use the 3-hour surface flux variable and surface albedo to get the downward shortwave flux and the reflected upward shortwave flux. Radiative flux variables at the top of atmosphere (TOA) are obtained directly from ERA-Interim. Total precipitation from ERA-Interim is used to calculate the latent heating. ERA-Interim also provides the environmental variables, SST, CWV, ω_{500}, which are used as the environmental variables that are matched with coupled CIPs.

2.3 Calculations of Coupled CIPs

Two coupled CIPs are calculated with the shortwave and longwave CRE from 2BFLX and the coincident CloudSat/AMSR-E precipitation. The radiative cooling efficiency, R_c, at the surface (SFC) is defined as:

$$Rc = \frac{F^{\downarrow}_{SW,SFC,all} - F^{\downarrow}_{SW,SFC,clear}}{LH} \quad (1)$$

where $F^{\downarrow}_{SW,SFC}$ is the downwelling shortwave (SW) flux that is evaluated in both clear-sky and all-sky conditions. Subscripts '*clear*' and '*all*' correspond to clear-sky and all-sky conditions respectively. R_c represents a cloud's ability to cool the surface per unit LH from rainfall, where LH is defined as the column latent heating from the precipitation reaching the surface and is calculated as

$$LH = \rho * L_v * RR \qquad (2)$$

where ρ is the density of water, L_v is latent heat of vaporization for water, and RR is the average surface rainfall rate from CloudSat or AMSR-E. Similarly, the atmospheric radiative heating efficiency R_h describes a cloud's ability to heat the atmosphere per unit LH,

$$R_h = \frac{(\Delta F_{LW} - \Delta F_{SW})_{all} - (\Delta F_{LW} - \Delta F_{SW})_{clear}}{LH} (3)$$

where $\Delta F_{LW} = F^{\uparrow}_{LW,SFC} - F^{\downarrow}_{LW,SFC} - F^{\uparrow}_{LW,TOA}$ and $\Delta F_{SW} = F^{\downarrow}_{SW,TOA} + F^{\uparrow}_{SW,SFC} - F^{\downarrow}_{SW,SFC} - F^{\uparrow}_{SW,TOA}$ are the longwave (LW) and SW atmospheric radiative flux divergence, respectively, calculated between the SFC and TOA. Clearly, you can see that the numerator of R_c is the cloud forcing at surface, that is, the amount of incoming solar radiation that has been hindered by the clouds. The numerator of R_h is the total CRE of the atmosphere, while the denominator of both equations is latent heating that has been released by the precipitation from the clouds.

We use 2BFLX to calculate the numerators of Equation (1) and Equation (3) during the daytime. The combination of 2C-RAIN-PROFILE and AMSR-E data provide surface precipitation rate from which we can estimate latent heating as in Equation (2). Again, due to the known limitations of the 2C-RAIN-PROFILE dataset in heavy rain scenarios, AMSR-E-CloudSat collocated products are used when the CPR is judged as saturated based on a flag in the algorithm. Otherwise, the CPR rain rate is used because CloudSat has a superior ability in detecting light and moderate rain (Behrangi et al. 2012; Lebsock et al. 2011).

Because the reanalysis precipitation is calculated based on the moisture budget and must meet the budget equilibrium, sometimes the precipitation has a rather small value in one grid box. As Stephens et al. (2010) discussed, models produce precipitation approximately twice as often as that observed and make too much light rainfall. The reanalysis products analyzed here provided values as small as 10^{-12} mm/hr, which is well below any space borne precipitation sensor detection limits and also produces unrealistically large values of R_c and R_h. Here we use the minimum precipitation value of 0.01 mm/hr for each grid box, which is the statistical minimum value of precipitation after sampling the CloudSat/AMSR-E precipitation for a grid box. This threshold is used to filter precipitation in reanalysis; however, we tested different thresholds and while there are expected changes in the quantitative value, the overall patterns and conclusions of this study are not dependent on the choice of threshold. To compare the different reanalysis datasets to each other and to the observations, we download ERA-Interim and MERRA-2 dataset at 2.5° x 2.5° directly with inherent interpolation. Meanwhile, all the A-Train data are also averaged to a common 2.5° x 2.5° grid at 3-hourly temporal resolution. Each pixel from A-Train datasets is matched to the nearest 3-hourly time step of the reanalysis datasets.

3. Global coupled CIPs distributions

An overview of the global distribution of coupled CIPs from A-Train, ERA-Interim and MERRA-2 is presented in Figure 1. These differ from the global patterns presented in Daloz et al. (2018) in a significant way. Daloz et al. (2018) used monthly-averaged radiation and precipitation to derive R_c and R_h. While these values are useful for identifying climatological biases that result from systematic differences in cloud and precipitation PDFs, at these long timescales radiation and precipitation may not be directly coupled. For example, it would be possible to capture the same monthly mean value of the coupled CIPs with compensating errors in the distribution of clouds and the wrong clouds producing precipitation. To more directly explore the connection between precipitation and radiation on the timescales of the clouds and the timescales for which the parameterizations must operate in the reanalyses, patterns of three hourly-averaged results are shown in Figure 1. They are similar to the patterns calculated from monthly mean fluxes, but differ in magnitude, since precipitation varies more temporally and spatially than the radiative flux. As a result, when R_c and R_h are calculated at shorter time scales, the variation of R_c and R_h is larger than that of the monthly average timescale shown in Daloz et al. (2018).

From A-Train observations, there are clear patterns that correspond to the global distribution of predominant cloud regimes. Generally, marine stratocumulus regions in the south and north Pacific and south or west Atlantic (Wood et al. 2012; Hartmann et al. 1993), where clouds cool the surface and atmosphere most efficiently because precipitation is weak, correspond to the strongest negative R_c and R_h. The Indo-Pacific warm pool region (white rectangle in Fig. 1) shows strong R_c and R_h, which means that deep convection cools the surface and heats the atmosphere more efficiently per unit rainfall. In shallow cumulus regions (180°W~135°W, 10°S~25°S), both R_c and R_h are weaker than other regions. Note that polar regions (beyond 60°N or 60°S), are removed due to the lack of liquid surface precipitation

(Stephen et al. 2008; L'Ecuyer et al. 2010; Lebsock and L'Ecuyer 2011; Mace et al. 2009; Mace et al. 2014) that results in too few samples in each grid box to provide meaningful results.

Comparison with ERA-Interim and MERRA-2 in Figure 1 shows the global patterns are generally consistent, although some tropical regions show significant differences between A-Train and the reanalyses. One of these main biases appears over the Indo-Pacific warm pool. Reanalyses generally fail to simulate both large R_c and R_h there. One possible reason, at least for ERA-Interim, is that it underestimates the LW CRE at TOA over tropical regions due to biases in cloud fraction and the TOA radiative flux diurnal cycles. Moreover, ERA-Interim overestimates precipitation in both ascending and descending regimes (Itterly et al 2014; Dolinar et al 2016). Fig 1c indicates that ERA-Interim R_c is generally stronger than other products over marine stratocumulus regions, which is likely caused by the SW biases reported by Dolinar et al. (2016). Meanwhile, Fig 1f illustrates that CloudSat and ERA-Interim R_h is generally more negative than MERRA-2 over marine stratocumulus regions, which is likely caused by underestimating the cloudiness over marine stratocumulus areas in MERRA-2 reported by Hinkelman (2019). Also, it has been reported that there is stronger water cycle in MERRA-2 than the observations because modifications in the MERRA-2 model resulted in changes in ocean evaporation and atmospheric transport and excessive precipitation is generated in the Indo-Pacific warm pool (Bosilovich et al. 2015; Bosilovich et al. 2017; Gelaro et al. 2017). This may also explain why MERRA-2 R_h is slightly smaller than ERA-Interim over the Indo-Pacific warm pool. Other differences appear over eastern Pacific marine stratocumulus region, where reanalyses generally produce stronger R_c over a larger region, which means that the clouds cool the surface more efficiently per unit rainfall. While reanalyses are constrained by observations, such biases may have significant implications for freely running GCMs since the regional variations in R_c and R_h feedback on the large-scale circulation. It also implies some limitations of models to represent the Walker and Hadley Circulations (L'Ecuyer et al. 2006).

As previously mentioned, due to the sampling limitations of the sun synchronous A-Train satellites, R_c and R_h values were only compared with reanalysis for grid boxes with satellite overpasses. While not shown here, R_c and R_h can be calculated from the full diurnal cycle available in the reanalyses. The climatological global patterns of the reanalyses are similar and still highly depend on the distributions of the cloud regimes, however the regional differences with observations are amplified with even weaker R_h and R_c in the warm pool and stronger R_h and R_c in subsidence regimes and the southern oceans.

Figure 2 demonstrates the time-scale dependence of R_c and R_h across daily to long-term (here 3 months) averaging time scales for the three different cloud regimes, deep convection, shallow cumulus, and stratocumulus, outlined in Figure 1. In each region, the absolute magnitude of both R_c and R_h decrease with increasing averaging time scales. At monthly or longer timescales, coupled CIP value are small and differences between the reanalyses and observations are also relatively small. However, as the averaging time scales decrease, the model-observational differences increase in most cloud regimes, but especially in the warm pool region. The top panels show that the precipitation-radiation coupling in deep convective regions, in particular, is not well-captured at the shorter time scales of the convection and both reanalyses have significantly weaker CIP than observed. The biases in greenhouse effect, surface SW CRE, and precipitation each also increase with averaging timescale (not shown), however, not to the degree of R_c and R_h. This suggests that these increasing biases with shorter averaging timescales are not due just radiation or precipitation, but rather their coupling in the reanalyses. Differences in the low cloud regimes are smaller, with the shallow cumulus regime showing similar but weaker patterns to deep convection. In stratocumulus regions, the biases are more constant with averaging timescale, likely representing the relatively persistent (in both space and time) cloud decks with little precipitation.

4. Environmental regime dependence

The previous figures indicate differences in the coupling between radiation and precipitation is associated with cloud regime. Because both cloud regimes (Bony et al. 2004) and precipitation, and correspondingly, the strength of latent heating have a strong relationship to the environment (Huaman and Schumacher 2017), to understand the drivers in the spatial patterns we analyze the relationship between coupled CIPs and several proxies often used to characterize synoptic environment, including both thermodynamic variables (SST and CWV) and dynamic variable (vertical pressure velocity at 500hpa (ω_{500}), which is a proxy for the large-scale overturning circulation).

The relationships between R_c and R_h and these environmental variables are shown in Figure 3. In the left panels, A-Train results show that R_c is relatively strong at low SSTs and then weakens (represented by an increase) with increasing SST until about 295-300 K. After this, R_c rapidly decreases with increasing SST representing a strong cooling efficiency enhancement. In the results of both reanalyses, the trends at moderate and high SSTs are completely opposite. At low SSTs they both show strengthening R_c, however R_c continues to become strong until SSTs reach around 295 K, at which point they rapidly weaken. One of the reasons for the lack of strong R_c in the reanalyses at high SSTs is that, as previously discussed, over the Indo-Pacific warm pool region, where SST is typically over 300 K, both reanalyses fail to simulate the strong R_c that is shown by A-Train. This suggests that the reanalyses do not accurately couple the storm-scale precipitation and cloud radiative effects at high SSTs, either producing too much precipitation or too weak shortwave cloud radiative forcing. Another difference is in the position of the first minimum, which occurs at similar SST for both reanalyses but occurs at a much lower SST for A-Train. This discrepancy results from the differences in the extent of the regions demonstrating relatively large R_c in A-Train and reanalysis. The position of the first minimum is determined by strong R_c over the marine stratocumulus region and mid-latitudes. Strong R_c over marine stratocumulus regions is confined to the Southern Ocean and regions along the coast where SSTs remain relatively low in the A-Train results. In the rest of subtropics and in the southern hemisphere extratropics, A-Train reports a lower R_c. The global distributions in Figure 1 show that regions of large R_c in reanalyses expand farther from the coasts toward the center of the ocean basins where SSTs are much warmer. However, reanalyses tend to produce lower cloud albedo and more precipitation over warmer SST regions. The differences combine make the R_c lower into regions of warmer SSTs. By contrast, the patterns of R_h associated with SSTs in the three datasets don't vary as much with R_h increasing with increasing SSTs. Reanalyses exhibit a relatively lower range although they switch from low clouds that cool the atmosphere to clouds that heat the atmosphere at different SSTs with A-Train falling in between the two reanalyses. In general, the reanalyses show more atmospheric cooling per unit rainfall at low SSTs associated with shallow, warm rain systems and less atmospheric heating at high SSTs, likely associated with deficiencies representing deeper and high cloud anvils or overestimating convective precipitation. The large differences between A-Train and the reanalyses simulating R_h at high SSTs is consistent with the differences shown over the warm pool area in Figure 1 and suggests that the reanalyses underestimate the strength of the coupling in deep convective cloud systems typical of this region.

In Figure 3c-d, the relationship between CWV and the coupled CIPs for the three datasets is shown. The patterns are similar to SST in all the three datasets, where R_c of A-Train has two minima but both reanalysis results only have one. It is not surprising that the results indicate the change in coupled CIPs with CWV is very similar to SST since the correlation coefficient between SST and CWV is 0.81 in ERA-Interim and 0.79 in MERRA2 in the matched dataset. However, from these plots, it is unknown which is the main driver. Many studies (Zhang et al. 1996; Bony et al. 2015; Trenberth et al. 2010) have shown a strong relationship between cloud radiative effects and SST, but studies also show a strong relationship between CWV and precipitation/latent heating (Bretherton et al. 2004; Peters and Neelin 2006; Neelin et al. 2009; Holloway and Neelin 2009; Ahmed and Schumacher 2015, 2016). However, from previous studies (Bony et al. 2004; Jakob et al. 2003; Jakob et al. 2005; Stephens 2005; Voigt and Shaw 2015), we know that both SST and CWV can contribute to the CRE and precipitation via different mechanisms, so a joint distribution of R_c and R_h with both variables is examined later in Figure 6 to determine which one is dominant in controlling R_c and R_h.

The link between coupled CIPs and dynamical regime is shown in Fig 3e-f. Figure 3e shows that R_c decreases as ω_{500} increases from negative (ascending regimes) to positive (subsidence regimes). Convective cloud regimes are generally associated with strong upward motion and typically accompanied by large precipitation and latent heat release, corresponding to a smaller R_c (assuming that the cloud forcing on the surface does not change). Positive ω_{500} is generally associated with a more stable atmosphere and the formation of low stratiform clouds where precipitation is usually small, but the cloud forcing on the surface could be very large leading to increased R_c. Both the observations and the reanalyses behave similarly, although they are closer in moderate ascending regimes than in subsidence regimes where A-Train results become much weaker than the two reanalysis estimates. Figure 3f shows that upward motion and downward motion obviously control the sign of R_h. For ascent regimes, R_h is positive and clouds heat the atmosphere more efficiently due to the enhancement of cloud greenhouse effect associated with deep convective clouds. For subsidence regimes, R_h is negative because the boundary layer tends to be more stable in these regimes and supports the formation of stratocumulus clouds, which will cool the atmosphere efficiently and produce little precipitation. Like R_c, the range of R_h estimates from A-Train and reanalyses appear to be closer in moderate ascent regimes than in the subsidence regimes and strong ascent regimes.

Given the large differences between observations and reanalyses in the tails of the curves in Figure 3, the relative frequency of occurrence in each environmental bin is shown in Figure 4. The ERA-Interim and MERRA2 distributions are quite similar suggesting the reanalyses produce atmospheric states with similar frequencies, although that is not necessarily indicative of how these states are coupled with precipitating convection and will be examined more later. There are clearly fewer samples in the tails of these distributions with few SST values above 302K or below 280K, few CWV values above 60 kg m^{-2} or below 10kg m^{-2}, and few ω_{500} values above 0.3 Pa/s and below -0.5 Pa/s. However, during data processing, we required a minimum of at least 100 samples for analysis and many of these bins still have hundreds to thousands of samples. While these environmental states are relatively rare and tend to be associated with very strong ascent or descent, they should not be neglected since they are often accompanied by some of the most extreme weather.

Given the strong covariability in SST, CWV, and dynamic regimes, it is not surprising that R_c and R_h appear to be influenced by more than one environment variable. In an attempt to determine which is the controlling variable, Figures 5 and 6 show the joint distributions of mean coupled CIPs conditionally sampled by combinations of different environmental variables. The first two rows of Fig. 5 show that the strength of R_c is largely controlled by the dynamic environment and that the observations and reanalyses are generally consistent. Clouds have strong cooling efficiencies in subsidence regimes and weak ones in ascent regimes. Within the ascent regime the observations show enhanced cooling with thermodynamic regime changes, while the reanalysis shows a steady weakening which appears to be more controlled by CWV than SST especially in MERRA-2. In the subsidence regimes, A-Train shows a steady weakening of R_c beginning at moderate SST and CWV, which is not shown in the reanalyses. This is likely due to the expansion of the regions of large R_c away from the coast and toward regions of greater SST and CWV shown by the reanalyses in Figure 1. The relationship between R_c and the thermodynamic environment echoes the considerable differences between A-Train observations and reanalyses shown in Figure 3. The reanalyses appear to be somewhat more horizontally stratified, which indicates that CWV is a stronger control on R_c than SST in the reanalyses compared to the observations. In the observations, below about 290K it is difficult to discern which thermodynamic variable is controlling R_c. For SST above 290K, holding SST fixed shows increasing R_c with CWV in observations and decreasing in reanalyses. Holding CWV fixed with increasing SST shows little variation in reanalyses, suggesting that CWV appears to control the strength of R_c. These results also indicate that the observations show much more distinction between the controls on cooling efficiencies in different cloud regimes, while the reanalyses vary much more smoothly from one regime to another.

R_h in Figure 6 shows that clouds have strong positive heating efficiencies in ascent regions and strong negative heating efficiencies in subsidence regimes. The sign of R_h is largely controlled by the dynamic environment, which is consistently shown in both A-Train observations and reanalyses. Within the ascent regime, A-Train results show an obvious trend in enhanced heating associated with the thermodynamic regime changes while the reanalysis show only a moderate enhanced heating, which is weakest in MERRA-2. This is likely due to the failure of reanalyses to simulate high R_h over warm pool regions as in Figure 1. From the last row of this figure, the observations demonstrate that clouds become increasingly efficient at heating the atmosphere per unit rain, especially in deep convective cloud regimes, in regions of ascent with high SST and CWV. The observations are also much more vertically stratified, indicating that CWV is a stronger control than SST in the observations compared to the reanalyses.

While Figure 5 shows that the reanalyses produce generally similar distributions of environments, Figure 3,5, and 6 suggest there are either differences in the environments in which the precipitating clouds occur or differences in the coupling between precipitation and radiation associated with a given atmospheric state in the reanalyses. Figure 7 shows the zonal mean difference (ERA-Interim minus MERRA-2) of air temperature, specific humidity, and ω profiles from the samples matched to A-Train precipitating clouds. While there are some hemispheric differences, the main patterns show that in the tropics and subtropics, ERA-Interim has a warmer temperature in the lower troposphere and lower temperature in the upper troposphere, suggesting a more stable atmosphere in MERRA-2. This is consistent with the negative omega differences across the tropics in Figure 7c, which means MERRA-2 has weaker ascent than ERA-Interim. In the subtropics where ω is typically positive, these negative differences mean MERRA-2 has stronger subsidence than ERA-Interim. The hemispheric differences in specific humidity are larger, but with the exception of the lower troposphere in the northern midlatitudes, the atmosphere is generally moister in MERRA-2. Along with the previous figures, this figure suggests that differences in the atmosphere in which convection occurs as well as how the precipitation-radiation coupling manifests in the various atmospheric states both contribute to the differences with observations. However, the environmental differences are relatively small and the differences between the observations (which have been matched to the reanalysis states) and reanalyses heating and cooling efficiencies in the previous figures suggests that the latter may be more important.

5. Summary and Discussions

In this paper, we use A-Train observations and reanalyses to study two coupled CIPs, R_c and R_h, that connect the surface and atmospheric CRE and precipitation. Not surprisingly, R_c and R_h vary with different cloud regimes. In regions dominated by stratocumulus clouds, they tend to cool the surface and atmosphere more efficiently per unit latent heat release because stratocumulus regions have low rain rates and highly reflective clouds that results in large cloud SW radiative forcing. In this situation, both strong SW CRE and low rain rate contribute to strengthen R_c. For regions associated with deep convective clouds in environments with strong ascent and sufficient CWV, observations show that clouds cool the surface and heat the atmosphere more efficiently per unit latent heat release than the regions where there is weak ascent or low CWV. Elevated and highly reflective cloud tops and large cirrus anvils enhance both the cloud greenhouse effect and the cloud SW radiative cooling at surface.

Comparison between A-Train observations and coupled CIPs in ERA-Interim and MERRA-2 show that they generally have similar global patterns. However, as model parameterizations are challenged with simulating different cloud regimes, we found some possible limitations of reanalysis data in coupling cloud radiative effects and precipitation over deep convective cloud regions. Both ERA-Interim and MERRA-2 show weaker R_c and R_h over the warm pool area where deep convective clouds prevail. The lower R_h values result from an underestimate of the LW CRE at TOA over tropical regions and overestimate of precipitation. Moreover, when the coupled CIPs are composited for increasingly shorter time scales, there are larger biases in reanalysis coupled CIPs compared with observation than was shown for calculations at longer timescales (Daloz et al. 2018), so we suspect that the reanalyses are challenged more in capturing the coupling between the radiation and precipitation for convective systems with shorter timescale variability, such as convectively-coupled waves.

Observation data inevitably have some uncertainties due to assumptions in the retrieval algorithms. For instance, 2BFLX partly overcomes the uncertainties in the radiative effects caused by low clouds, cirrus and aerosols, but some uncertainties remain in the SW and LW fluxes. The former is primarily the result of uncertainties in LWC estimates, and the latter is linked to errors in prescribed skin temperature and the lower-tropospheric water vapor (Henderson et al. 2013). These uncertainties should be considered when comparing observational results and reanalysis or model outputs; however, Henderson et al. (2013) showed relatively good agreement between CERES and 2BFLX although it should be noted that differences become relatively larger at shorter temporal and smaller spatial averaging scales. Estimates from different observation systems in the future could help reduce these observational uncertainties.

How coupled CIPs are linked with their environment was also examined. Generally, the reanalyses show less heating of the atmosphere at high SSTs and more cooling of the atmosphere at low SSTs. The dynamic regime appears to act as a switch with weak to strong surface cooling efficiencies and from atmospheric cooling to heating as the regime shifts from ascent to subsidence. The thermodynamic regime acts more as a control on the strength of the coupling parameters, especially for R_h. In ascent regimes, precipitating clouds go from weak to strong R_h

with increasing SST and CWV which suggests that cloud heat the atmosphere more efficiently per unit rainfall in warm and moist environments. Joint distributions of R_h as a function of SST and CWV in the observations indicate that CWV is the primary control, with relatively constant R_h across a range of SSTs (between 275K-302K) for fixed CWV. Reanalyses capture the general relationships between coupled CIPs and their environment, with several important distinctions. Neither ERA-Interim or MERRA-2 capture the strong cooling efficiencies at high SST and CWV, instead they have strong R_c from low to moderate SST and CWV which rapidly weakens at high SST and CWV suggesting that the coupling between precipitation and shortwave cloud forcing in these regimes is too weak in the reanalyses. Likewise, reanalyses also fail to capture the strong heating per unit precipitation with increasing SST and CWV. They also do not appear to be as strongly linked with the environmental moisture as the observations.

The observational-reanalyses discrepancies shown here could be caused by a variety of factors including differences in the environmental states in which convection occurs in the reanalyses, differences in the timing and location of reanalysis convection (leading to mismatches with the observations at the shorter timescales examined here), or the precipitation-radiation coupling produced by the model parameterizations. There are notable differences in the environments in which the two reanalyses produce convection which may explain some of the differences between the two reanalyses. However, there are still clear differences between the observations and the reanalyses when the observations are composited by the reanalysis environmental states which suggests the latter two factors could play a bigger role. Attempting to correct timing and location mismatches for every precipitating cloud is beyond the scope of this study, but there are clear indications in the literature that suggest the biases of R_c and R_h between the reanalysis and observations may be linked to both uncertainties in the representation of cloudiness and precipitation intensity, as well as how they are coupled in the reanalysis systems. Both Miao et al. (2019) and Hinkelman. (2019) show that in tropical regions, ERA-Interim exhibits considerable underestimation for high-level clouds, which reduces both the SW and LW CRE at TOA. However, MERRA-2 better represents high-level clouds, perhaps even overrepresents, but tends to underestimate the middle and low-level cloudiness. In MERRA-2's case, the biases of R_c and R_h may be mainly due to the excessive convective precipitation intensity over the warm pool region (Bosilovich et al. 2017). Given the lack of middle and low-level cloudiness, there may also be some biases in radiative fluxes due to cloud thickness. In addition to the potential underestimation in high clouds in ERA-Interim, it may overestimate precipitation in both ascending and descending regimes related to the parameterization scheme used in both convective and marine boundary layer clouds (Dolinar et al 2016) and not capturing the cloud entrainment and detrainment rates (Naud et al. 2014). Fortunately, in the latest version ERA-5 (Hersbach et al 2018), representations of mixed phased clouds and parameterization of convection including entrainment and coupling with large-scale circulation are expected to be improved leading better estimates of convective cloudiness, radiation at TOA, and precipitation.

Even though over most of the globe, R_h and R_c are not large, Daloz et al. (2018) highlight the importance of R_h and R_c in regions such as the west Pacific Ocean and mid-Atlantic. For example, in failing to simulate R_c and R_h over the Indo-Pacific warm pool, reanalysis also does not capture a strong enough of east-west gradient of R_c and R_h over the Pacific as in the A-Train results. However, as the transition of the precipitation gradient over the Pacific becomes more pronounced during an ENSO event, the model response to the circulation becomes more sensitive to the latent heating variation (Schumacher et al. 2004). Also, a slight change in surface fluxes and tropospheric moistening over the West Pacific Ocean could have significant influence on the propagation of MJO that may not be captured in reanalysis or models given the increasingly large biases between reanalyses and observations at shorter coupling timescales. Daloz et al (2018) also suggested that R_h may be a good proxy for processes associated convective aggregation. Compensating subsidence around more aggregated convection will make the surrounding atmosphere drier and clearer and increase outgoing longwave radiation to the space (Bretherton et al. 2005; Tobin et al. 2012; Bony et al. 2015; Daloz et al 2018). In our observational results, R_h is high over the warm pool area and generally increases in regions of high CWV and SST, which indicates that the atmospheric radiative heating by deep convection increases faster than the precipitation power law scaling with CWV that has been shown in a number of studies (Bretherton et al. 2004, Ahmed and Schumacher 2015). This could imply that cloud systems vary in such a way, perhaps via convective aggregation in moist regions, as to become more efficient at heating the atmosphere per unit rainfall to maintain global energy balance with the expanding dry regions.

In the future, the coupled CIPs can be compared with those in GCMs or cloud resolving models to understand how well models couple precipitation and radiation, what parameterizations need to be improved to better capture the coupling, and determine more about the underlying physical processes driving the observed relationships between coupled CIPs and their environment.

Acknowledgments

We appreciate the helpful comments and suggestions of three anonymous reviewers, and Dr. Schumacher in Department of Atmospheric Sciences, Texas A&M University, which improved this manuscript considerably. This research is supported by NASA energy and water cycle study (NEWS) Grant NNX15AD13G. The CloudSat data were downloaded from the CloudSat processing center (http://www.cloudsat.cira.colostate.edu/). The AMSR-E Rainfall Subset collocated with CloudSat track were downloaded from Goddard Earth Science Data and Information Services Center (http://disc.sci.gsfc.nasa.gov/datacollection/AMSRERR_CPR_V002.html). ERA-Interim data were obtained from the European Centre for Medium-Range Weather Forecasts (http://apps.ecmwf.int/datasets/). MERRA-2 data were provided by the Goddard Earth Sciences Data and Information Services Center (https://disc.gsfc.nasa.gov/daac-bin/FTPSubset2.pl). All datasets used in this analysis are open access.

References

Ahmed, F., and C. Schumacher, 2015: Convective and stratiform components of the precipitation-moisture relationship. Geophys. Res. Lett., 42, 10 453–10 462, doi:10.1002/2015GL066957.

Ahmed, F., C. Schumacher, Z. Feng, and S. Hagos, 2016: A retrieval of tropical latent heating using the 3D structure of precipitation features. J. Appl. Meteor. Climatol., 55, 1965–1982, https://doi.org/10.1175/JAMC-D-15-0038.1.

Allan, R. P., 2009: Examination of relationships between clear-sky longwave radiation and aspects of the atmospheric hydrological cycle in climate models, reanalyses, and observations. J. Climate, 22, 3127–3145, doi:10.1175/2008JCLI2616.1.

Allan, R. P.,2011: Combining satellite data and models to estimate cloud radiative effect at the surface and in the atmosphere. Meteor. Appl., 18, 324–333

Andrew, T., P.M.Forster, O. Boucher, N. Bellouin, and A. Jones, 2010: Precipitation, radiative forcing and global temperature change. Geophys. Res. Lett., 37, L14701, doi:10.1029/2010GL043991.

Bacmeister, J. T. and Stephens, G.: Spatial statistics of likely convective clouds in CloudSat data, J. Geophys. Res., 116, D04104, doi:10.1029/2010JD014444, 2011.

Behrangi, A., M. Lebsock, S. Wong, and B. Lambrigtsen, 2012: On the quantification of oceanic rainfall using spaceborne sensors. J. Geophys. Res., 117, D20105, https://doi.org/10.1029/2012JD017979.

Behrangi, A., Y. Tian, B. H. Lambrigtsen, and G. L. Stephens, 2014b: What does CloudSat reveal about global land precipitation detection by other spaceborne sensors? Water Resour. Res., 50, 4893–4905, doi:10.1002/2013WR014566.

Betts A. K., R. Desjardins, D. Worth, and B. Beckage, 2014: Climate coupling between temperature, humidity, precipitation, and cloud cover over the Canadian Prairies. J. Geophys. Res. Atmos., 119, 13 305–13 326, doi:10.1002/2014JD022511.

Bodas-Salcedo, A., M. J. Webb, M. E. Brooks, M. A. Ringer, K. D. Williams, S. F. Milton, and D. R.Wilson, 2008: Evaluating cloud systems in the Met Office global forecast model using simulated CloudSat radar reflectivities. J. Geophys. Res.,113, D00A13, doi:https://doi.org/10.1029/2007JD009620.

Bony S, Dufresne JL, Le Treui H, Morcrette JJ, Snior C (2004) On dynamic and thermodynamic components of cloud changes. Clim Dyn 22:71–86. doi:10.1007/s00382-003-0369-6

Bony S, and Coauthors, 2015: Clouds, circulation and climate sensitivity. Nat. Geosci., 8, 261–268, doi:https://doi.org/10.1038/ngeo2398.

Bony S, and J. Dufresne, 2005: Marine boundary layer clouds at the heart of tropical cloud feedback uncertainties in climate models. Geophys. Res. Lett., 32, L20806, https://doi.org/10.1029/2005GL023851.

Bosilovich, M. G., and Coauthors, 2015b: MERRA-2: Initial evaluation of the climate. NASA/TM-2015-104606, Vol. 43, 139 pp.

Bosilovich, M. G., R. Lucchesi, and M. Suarez, 2016: MERRA-2: File specification. GMAO Office Note 9, 73 pp. [Available online at https://gmao.gsfc.nasa.gov/pubs/docs/Bosilovich785.pdf.]

Bosilovich, M. G., F. Robertson, L. Takacs, A. Molod, and D. Mocko, 2017: Atmospheric water balance and variability in the MERRA-2 reanalysis. J. Climate, 30, 1177–1196, doi:https://doi.org/10.1175/JCLI-D-16-0338.1.

Bouniol, D., R. Roca, T. Fiolleau, and E. Poan, 2016: Macrophysical, microphysical, and radiative properties of tropical mesoscale convective systems along their life cycle. J. Climate, 29, 3353–3371, doi:10.1175/JCLI-D-15-0551.1.

Bretherton, C.S. and A.H. Sobel, 2002: A Simple Model of a Convectively Coupled Walker Circulation Using the Weak Temperature Gradient Approximation. J. Climate, 15,2907–2920, https://doi.org/10.1175/1520-0442(2002)015<2907:ASMOAC>2.0.CO;2

Bretherton, C.S., C. S., M. E. Peters, and L. E. Back, 2004: Relationships between water vapor path and precipitation over the tropical oceans. J. Climate, 17, 1517–1528.

Bretherton, C.S., P. N. Blossey, and M. Khairoutdinov, 2005: An energy-balance analysis of deep convective self-aggregation above uniform SST. J. Atmos. Sci., 62, 4273–4292, https://doi.org/10.1175/JAS3614.1.

Calisto, M., D. Folini, M. Wild, and L. Bengtsson, 2014: Cloud radiative forcing intercomparison between fully coupled CMIP5 models and CERES satellite data. Ann. Geophys., 32, 793–807, doi:10.5194/angeo-32-793-2014.

Ceppi, P., F. Brient, M. D. Zelinka, and D. L. Hartmann, 2017: Cloud feedback mechanisms and their representation in global climate models. Wiley Interdiscip. Rev.: Climate Change, 8, e465, https://doi.org/10.1002/wcc.465.

Choi, Y.-S., C.-H. Ho, C.-E. Park, T. Storelvmo, and I. Tan, 2014: Influence of cloud phase composition on climate feedbacks. J. Geophys. Res. Atmos., 119, 3687–3700, doi: https://doi.org/10.1002/2013JD020582

Clark A.J., W.A.Gallus Jr., and T.-C. Chen (2007) Comparison of the Diurnal Precipitation Cycle in Convection-Resolving and Non-Convection-Resolving

Mesoscale Models. Mon. Wea. Rev., 135, 3456–3473, https://doi.org/10.1175/MWR3467.1

Colman, R. A., 2015: Climate radiative feedbacks and adjustments at the Earth's surface. J. Geophys. Res. Atmos., 120, 3173– 3182, doi:10.1002/2014JD022896.

Cullather, R. I., S. M. J. Nowicki, B. Zhao, and M. J. Suarez, 2014: Evaluation of the surface representation of the Greenland ice sheet in a general circulation model. J. Climate, 27, 4835–4856, https://doi.org/10.1175/JCLI-D-13-00635.1.

Dai, A., and K. E. Trenberth, 2004: The diurnal cycle and its depiction in the Community Climate System Model. J. Climate, 17, 930–951, https://doi.org/10.1175/1520-0442(2004)017<0930:TDCAID>2.0.CO;2.

Dai, F., R. Yu, X. Zhang, Y. Yu, and J. Li, 2003: The impact of low-level cloud over the eastern subtropical Pacific on the "double ITCZ" in LASG FGCM-0. Adv. Atmos. Sci., 20, 461–474, doi:https://doi.org/10.1007/BF02690804.

Daloz, A., E. Nelson, T. L'Ecuyer, A. Rapp, and L. Sun, 2018: Assessing the coupled influences of clouds on the Atmospheric Energy and Water Cycles in Reanalyses with A-Train Observations. J. Climate. doi:10.1175/JCLI-D-17- 0862.1.

Dee D. P., Uppala S. M., Simmons A. J., Berrisford P., Poli P., Kobayashi S., Andrae U., Balmaseda M. A., Balsamo G., Bauer P., Bechtold P., Beljaars A. C. M., van de Berg L., Bidlot J., Bormann N., Delsol C., Dragani R., Fuentes M., Geer A. J., Haimberger L., Healy S. B., Hersbach H., Hólm E. V., Isaksen L., Kållberg P., Köhler M., Matricardi M., McNally A. P., Monge-Sanz B. M., Morcrette J.-J., Park B.-K., Peubey C., de Rosnay P., Tavolato C., Thépaut J.-N. and Vitart, F.

(2011) The ERA-Interim reanalysis: configuration and performance of the data assimilation system. Q.J.R. Meteorol. Soc., 137: 553–597. doi: 10.1002/qj.828

Dessler, A. E., 2010: A determination of the cloud feedback from climate variations over the past decade. Science, 330, 1523–1527, doi:10.1126/science.1192546

Dinh, T. and S. Fueglistaler, 2017: Mechanism of fast atmospheric energetic equilibration following radiative forcing by CO_2. J. Adv. Model. Earth Syst., 9, 2468–2482. doi: https://doi.org/10.1002/2017MS001116

Dolinar E.K., Dong X. and Xi B. (2016): Evaluation and Intercomparison of clouds, precipitation and radiation budgets in recent reanalyses using satellite-surface observations. Clim. Dyn. 46:2123-2144. doi: 10.1007/s00382-015-2693-z.

Eitzen, Z., K. Xu, and T. Wong, 2011: An estimate of low-cloud feedbacks from variations of cloud radiative and physical properties with sea surface temperature on interannual time scales. J. Climate, 24, 1106–1121, doi:https://doi.org/10.1175/2010JCLI3670.1.

Gelaro, R., W. McCarty, M.J. Suárez, R. Todling, A. Molod, L. Takacs, C.A. Randles, A. Darmenov, M.G. Bosilovich, R. Reichle, K. Wargan, L. Coy, R. Cullather, C. Draper, S. Akella, V. Buchard, A. Conaty, A.M. da Silva, W. Gu, G. Kim, R. Koster, R. Lucchesi, D. Merkova, J.E. Nielsen, G. Partyka, S. Pawson, W. Putman, M. Rienecker, S.D. Schubert, M. Sienkiewicz, and B. Zhao, 2017: The Modern-Era Retrospective Analysis for Research and Applications, Version 2 (MERRA-2). J. Climate, 30, 5419–5454,https://doi.org/10.1175/JCLI-D-16-0758.1

Global Hydrology Resource Center/MSFC/NASA (2009), AMSR-E L2 Rainfall Subset, collocated with CloudSat track V002, Edited by GES DISC, Greenbelt, MD, USA, Goddard Earth Sciences Data and Information Services Center (GES DISC), Accesse: 09-01-2017, https://disc.gsfc.nasa.gov/datacollection/AMSRERR_CPR_002.html

Grabowski, W. W., Bechtold, P., Cheng, A., Forbes, R., Halliwell, C., Khairoutdinov, M., Lang, S., Nasuno, T., Petch, J., Tao, W.-K., Wong, R., Wu, X. and Xu, K.-M. (2006), Daytime convective development over land: A model intercomparison based on LBA observations. Q.J.R. Meteorol. Soc., 132: 317–344. doi:10.1256/qj.04.147

Griggs, J., and J. Bamber, 2008: Assessment of cloud cover characteristics in satellite datasets and reanalysis products for Greenland. *J. Climate*, **21**, 1837–1849.

Haynes, J. M., and G. L. Stephens (2007), Tropical oceanic cloudiness and the incidence of precipitation: Early results from CloudSat, Geophys. Res. Lett., 34, L09811, doi:10.1029/2007GL029335.

Haynes, J. M., T. S. L'Ecuyer, G. L. Stephens, S. D. Miller, C. Mitrescu, N. B. Wood, and S. Tanelli, 2009: Rainfall retrieval over the ocean with spaceborne W-band radar. J. Geophys. Res., 114, D00A22, doi:10.1029/2008JD009973.

Held, I. M., and B. J. Soden, 2006: Robust responses of the hydrological cycle to global warming. J. Climate, 19, 5686–5699, https://doi.org/10.1175/JCLI3990.1.

Henderson, D.S., T. L'Ecuyer, G. Stephens, P. Partain, and M. Sekiguchi, 2013: A Multisensor Perspective on the Radiative Impacts of Clouds and Aerosols. J. Appl. Meteor. Climatol., 52, 853–871, doi:10.1175/JAMC-D-12-025.1.

Hersbach, H., P. de Rosnay, B. Bell, D. Schepers, A. Simmons, C. Soci, S. Abdalla, M. Alonso Balmaseda, G. Balsamo, P. Bechtold, P. Berrisford, J. Bidlot, E. de Boisséson, M. Bonavita, P. Browne, R. Buizza, P. Dahlgren, D. Dee, R. Dragani, M. Diamantakis, J. Flemming, R. Forbes, A. Geer, T. Haiden, E. Hólm, L. Haimberger, R. Hogan, A.

Horányi, M. Janisková, P. Laloyaux, P. Lopez, J. Muñoz-Sabater, C. Peubey, R. Radu, D. Richardson, J.-N. Thépaut, F. Vitart, X. Yang, E. Zsótér & H. Zuo, 2018: Operational global reanalysis: progress, future directions and synergies with NWP, ECMWF ERA Report Series 27

Hinkelman, L.M., 2019: The Global Radiative Energy Budget in MERRA and MERRA-2: Evaluation with Respect to CERES EBAF Data. J. Climate, 32, 197301994, https://doi.org/10.1175/JCLI-D-18-0445.1

Holloway, C. E., and J. D. Neelin, 2009: Moisture vertical structure, column water vapor, and tropical deep convection. J. Atmos. Sci., 66, 1665–1683, doi:10.1175/2008JAS2806.1.

Huaman, L., C. Schumacher, 2017: Assessing the vertical latent heating structure of the East Pacific ITCZ using the CloudSat CPR and TRMM CPR. J. Climate, 31, 2563-2577, doi: 10.1175/JCLI-D-17-0590.1

Itterly, K. F., and P. C. Taylor, 2014: Evaluation of the tropical TOA flux diurnal cycle in MERRA and ERA-Interim retrospective analyses. J. Climate, 27, 4781–4796, doi:10.1175/ JCLI-D-13-00737.1.

Jakob, C. and Klein, S. A. (2000), A parametrization of the effects of cloud and precipitation overlap for use in general-circulation models. Q.J.R. Meteorol. Soc., 126: 2525–2544. doi:10.1002/qj.49712656809

Jakob, C., and G. Tselioudis, 2003: Objective identification of cloud regimes in the tropical western Pacific. Geophys. Res. Lett., 30, 2082, doi:10.1029/2003GL018367.

Jakob, C., G. Tselioudis, and T. Hume, 2005: The radiative, cloud, and thermodynamic properties of the major tropical western Pacific cloud regimes. J. Climate, 18, 1203–1215.

Kay, J., and Coauthors, 2012: Exposing global cloud biases in the Community Atmosphere Model (CAM) using satellite observations and their corresponding instrument simulators. J. Climate, 25, 5190–5207, doi:https://doi.org/10.1175/JCLI-D-11-00469.1.

Kim, D., M.-S. Ahn, I.-S. Kang, and A. D. Del Genio, 2015: Role of longwave cloud–radiation feedback in the simulation of the Madden–Julian oscillation. J. Climate, 28, 6979–6994, doi:10.1175/ JCLI-D-14-00767.1.

Kim, J. and M.J. Alexander, 2013: Tropical Precipitation Variability and Convectively Coupled Equatorial Waves on Sub-monthly Time Scales in Reanalyses and TRMM. J. Climate, 26, 3013–3030, https://doi.org/10.1175/JCLI-D-12-00353.1

Klein, S. A., and D. L. Hartmann, 1993: The seasonal cycle of low stratiform clouds. *J. Climate*, **6**, 1587–1606, doi:https://doi.org/10.1175/1520-0442(1993)006<1587:TSCOLS>2.0.CO;2.

Kohler M., Ahlgrimm M., Beljaars A.C.M. (2011) Unified treatment of dry convective and stratocumulus-topped boundary layers in the ECMWF model. Q.J.R. Meteo. Sci. 137:43-57.

Kubar, T. L., D. E. Waliser, J. L. Li, and X. Jiang, 2012: On the annual cycle, variability, and correlations of oceanic lowtopped clouds with large-scale circulation using Aqua MODIS and ERA-Interim. J. Climate, 25, 6152–6174, doi:10.1175/JCLI-D-11-00478.1.

Kummerow, C. D., S. Ringerud, J. Crook, D. Randel, and W. Berg, 2011: An observationally generated a priori database for microwave rainfall retrievals. J. Atmos. Oceanic Technol., 28, 113–130, doi:10.1175/2010JTECHA1468.1.

Kummerow, C. D., D. L. Randel, M. Kulie, N-Y. Wang, R. Ferraro, S. J. Munchak, and V. Petkovic, 2015: The evolution of the Goddard profiling algorithm to a fully parametric scheme. J. Atmos. Oceanic Technol., doi:10.1175/JTECH-D-15-0039.1

Larson, K., and D. L. Hartmann and S. A. Klein, 1999: The role of clouds, water vapor, circulation, and boundary layer structure in the sensitivity of the tropical climate. J. Climate, 12, 2359–2374.

Larson, K., and D. L. Hartmann, 2003: Interactions among cloud, water vapor, radiation, and large-scale circulation in the tropical climate. Part I: Sensitivity to uniform sea surface temperature changes. J. Climate, 16, 1425–1440.

Larson, K., and D. L. Hartmann, 2003: Interactions among cloud, water vapor, radiation, and large-scale circulation in the tropical climate. Part II: Sensitivity to spatial gradients of sea surface temperature. J. Climate, 16, 1441–1455.

Lee, M.-I, I.-S. Kang, J.-K. Kim, and B. E. Mapes, 2001: Influence of cloud-radiation interaction on simulating tropical intraseasonal oscillation with an atmospheric general circulation model. J. Geophys. Res. 106, 14219-14233.

Lebsock, M. D., and T. S. L'Ecuyer, 2011: The retrieval of warm rain from CloudSat. J. Geophys. Res., 116, D20209, https://doi.org/10.1029/2011JD016076.

Lebsock, M. D., and T. S. L'Ecuyer, D. Vane, G. Stephens, and D. Reinke, 2011: Level 2C RAIN-PROFILE product process description and interface control document, algorithm version 0.0. JPL Rep., 14 pp., http://www.cloudsat.cira.colostate.edu/sites/default/files/products/files/2C-RAIN-PROFILE-PDICD.P_R04.20110620.pdf.

Level 2B Fluxes and Heating Rates and 2B Fluxes and Heating Rates w/ Lidar Process Description and Interface Control Document, CloudSat Team, 2006.

L'Ecuyer, T. S., H. Masunaga, and C. Kummerow, 2006: Variability in the characteristics of precipitation systems in the tropical Pacific. Part II: Implications for atmospheric heating. J. Climate, 19, 1388–1406.

L'Ecuyer, T. S., and G. L. Stephens, 2007: The Tropical Atmospheric Energy Budget from the TRMM Perspective. Part II: Evaluating GCM Representations of the Sensitivity of Regional Energy and Water Cycles to the 1998-99 ENSO Cycle, J. Climate 20, 4548-4571.

L'Ecuyer, T. S., N.B. Wood, T. Haladay, G.L. Stephens, and P.W. Stackhouse Jr., 2008: Impact of clouds on atmospheric heating based on the R04 CloudSat fluxes and heating rates dataset. J. Geophys. Res., 113, D00A15, doi:10.1029/2008JD009951.

L'Ecuyer, T. S., and J.H. Jiang, 2010: Touring the atmosphere aboard the A-Train. Phys. Today, 63, 36–41, doi:10.1063/1.3463626.

Li, J. L., X. H. Zhang, Y. Q. Yu, and F. S. Dai, 2004: Primary reasoning behind the double ITCZ phenomenon in a coupled ocean-atmosphere general circulation model. Adv. Atmos. Sci., 21, 857–867, doi:https://doi.org/10.1007/BF02915588.

Liu, Y., and J. R. Key, 2016: Assessment of Arctic cloud cover anomalies in atmospheric reanalysis products using satellite data. J. Climate, **29**, 6065–6083, https://doi.org/10.1175/JCLI-D-15-0861.1.

Liu, Y., and Q. Zhang, 2014: The CloudSat radar–lidar geometrical profile product (RL-GeoProf): Updates, improvements, and selected results. J. Geophys. Res. Atmos., 119, 9441–9462, doi:https://doi.org/10.1002/2013JD021374.

Mace, G. G., and S. Benson, 2017: Diagnosing cloud microphysical process information from remote sensing measurements—A feasibility study using aircraft data. Part I: Tropical anvils measured during TC4. J. Appl. Meteor. Climatol., 56, 633–649, doi:https://doi.org/10.1175/JAMC-D-16-0083.1.

Mace, G. G., and Q. Zhang, 2014: The CloudSat radar–lidar geometrical profile product (RL-GeoProf): Updates, improvements, and selected results. J. Geophys. Res. Atmos., 119, 9441–9462, doi:10.1002/2013JD021374.

Mace, G. G., Q. Zhang, M. Vaughan, R. Marchand, G. Stephens, C. Trepte, and D. Winker, 2009: A description of hydrometeor layer occurrence statistics derived from the first year of merged CloudSat and CALIPSO data. J. Geophys. Res., 114, D00A26, doi:10.1029/2007JD009755.

Masunaga, H., and T. S. L'Ecuyer, 2011: Equatorial asymmetry of the east Pacific ITCZ: Observational constraints on the underlying processes. J. Climate, 24, 1784–1800, doi:https://doi.org/10.1175/2010JCLI3854.1.

Miao, H, Wang, X, Liu, Y, Wu, G. An evaluation of cloud vertical structure in three reanalyses against CloudSat/cloud-aerosol lidar and infrared pathfinder satellite observations. Atmos Sci Lett. 2019; 20:e906. https://doi.org/10.1002/asl.906

Mlawer E.J., Taubman S.J., Brown P.D., Iacono M.J., Clough S.A. (1997) Radiative transfer for inhomogeneous atmospheres: RRTM, a validated correlated-k model for the longwave. J. Geophys. Res. 102D:16663-16682.

Molod A., L. Takacs, M.Suarez and J. Bacmeister, 2015: Development of the GEOS-5 general circulation model: evolution from MERRA to MERRA2. Geosc. Model. Ev., 8, 1339-1356.

Moorthi, S., and M. J. Suarez, 1992: Relaxed Arakawa–Schubert: A parameterization of moist convection for general circulation models. Mon. Wea. Rev., 120, 978–1002, doi:https://doi.org/10.1175/1520-0493(1992)120<0978:RASAPO>2.0.CO;2.

Muller, C. J., and I. M. Held, 2012: Detailed investigation of the self-aggregation of convection in cloud-resolving simulations. J. Atmos. Sci., 69, 2551–2565, https://doi.org/10.1175/JAS-D-11-0257.1.

Muller, C. J., and S. Bony, 2015: What favors convective aggregation and why? Geophys. Res. Lett., 42, 5626–5634, doi:10.1002/2015GL064260.

Naud, C. M., J. F. Booth, and A. D. Del Genio, 2014: Evaluation of ERA-Interim and MERRA cloudiness in the Southern Ocean. J. Climate, 27, 2109–2124, https://doi.org/10.1175/JCLI-D-13-00432.1.

Neelin, J. D., O. Peters, and K. Hales, 2009: The transition to strong convection. J. Atmos. Sci., 66, 2367–2384, doi:10.1175/ 2009JAS2962.1.

Nguyen, H., A. Evans, C. Lucas, I. Smith, and B. Timbal, 2013: The Hadley circulation in reanalyses: Climatology, variability, and change. J. Climate, 26, 3357–3376, https://doi.org/10.1175/ JCLI-D-12-00224.1.

O'Brien, T. A., F. Li, W. D. Collins, S. A. Rauscher, T. D. Ringler, M. A. Taylor, S. M. Hagos, and L. R. Leung, 2013: Observed scaling in clouds and precipitation and scale incognizance in regional to global atmospheric models. J. Climate, 26, 9313– 9333, doi:10.1175/JCLI-D-13-00005.1.

O'Gorman, P. A., R. P. Allan, M. P. Byrne, and M. Previdi, 2012: Energetic constraints on precipitation under climate change. Surv. Geophys., 33, 585–608, doi:10.1007/ s10712-011-9159-6.

Pendergrass, A. G., and D. L. Hartmann, 2014: The atmospheric energy constraint on global-mean precipitation change. J. Climate, 27, 757–768, doi:https://doi.org/10.1175/JCLI-D-13-00163.1.

Peters, O., and J. D. Neelin, 2006: Critical phenomena in atmospheric precipitation. Nat. Phys., 2, 393–396.

Previdi, M., 2010: Radiative feedbacks on global precipitation. Environ. Res. Lett., 5, 025211, doi:10.1088/1748-9326/5/2/025211.

Rädel, G., T. Mauritsen, B. Stevens, D. Dommenget, D. Matei, K. Bellomo, and A. Clement, 2016: Amplification of El Niño by cloud longwave coupling to atmospheric circulation. Nat. Geosci., 9, 106–110, https://doi.org/10.1038/ngeo2630.

Randall, D. and Coauthors, 2007: Climate models and their evaluation. Climate Change 2007: The Physical Science Basis. Contribution of Working Group I to the Fourth Assessment Report of the Intergovernmental Panel on Climate Change, S. Solomon, D. Qin, M. Manning, Z. Chen, M. Marquis, K. Averyt, M. Tignor, and H. Miller, Eds., Cambridge University Press, Cambridge, 589-662.

Ritter, B., and J.-F. Geleyn, 1992: A comprehensive radiation scheme for numerical weather prediction models with potential applications in climate simulations. *Mon. Wea. Rev.*, **120**, 303–325, https://doi.org/10.1175/1520-0493(1992)120<0303:ACRSFN>2.0.CO;2.

Schumacher, C., R. A. Houze Jr., and I. Kraucunas, 2004: The tropical dynamical response to latent heating estimates derived from the TRMM precipitation radar. J. Atmos. Sci., 61, 1341–1358, https://doi.org/10.1175/1520-0469(2004)061,1341: TTDRTL.2.0.CO;2.

Sobel and H. Gildor, 2003: A simple time-dependent model of SST hot spots. J. Climate, 16, 3978–3992.

Song, X., and G. Zhang, 2009: Convection parameterization, tropical Pacific double ITCZ, and upper-ocean biases in the NCAR CCSM3. Part I: Climatology and atmospheric feedback. J. Climate, 22, 4299–4315, doi:https://doi.org/10.1175/2009JCLI2642.1.

Stengel, M., Schlundt, C., Stapelberg, S., Sus, O., Eliasson, S., Willén, U., and Meirink, J. F.: Comparing ERA-Interim clouds with satellite observations using a simplified satellite simulator, Atmos. Chem. Phys. Discuss., https://doi.org/10.5194/acp-2018-258, in review, 2018

Stephens, G., 2005: Cloud feedbacks in the climate system: A critical review. J. Climate, 18, 237–273, doi:10.1175/JCLI-3243.1.

Stephens, G., and Coauthors, 2008: CloudSat mission: Performance and early science after the first year of operation. J. Geophys. Res., 113, D00A18, doi:10.1029/2008JD009982.

Stephens, G., and T. D. Ellis, 2008: Controls of global-mean precipitation increases in global warming GCM experiments. J. Climate, 21, 6141-6155, https://doi.org/10.1175/2008JCLI2144.1.

Stephens, G., and Coauthors, 2010: Dreary state of precipitation in global models. J. Geophys. Res., 115, D24211, doi:10.1029/2010JD014532.

Stephens, G., D. Winker, J. Pelon, C. Trepte, D. Vane, C. Yuhas, T. L'Ecuyer, and M. Lebsock, 2017: CloudSat and CALIPSO within the A-Train: Ten years of actively observing the Earth system. Bull. Amer. Meteor. Soc., 0, https://doi.org/10.1175/BAMS-D-16-0324.1

Sassen, K., Z. Wang, and D. Liu, 2008: The global distribution of cirrus clouds from CloudSat/Cloud–Aerosol Lidar and Infrared Pathfinder Satellite Observations (CALIPSO) measurements. J. Geophys. Res., 113, D00A12, doi:10.1029/ 2008JD009972

Stevens, B., and S. Bony, 2013: What are climate models missing? Science, 340, 1053–1054, https://doi.org/10.1126/science.1237554.

Kociuba, G., and S. B. Power, 2015: Inability of CMIP5 models to simulate recent strengthening of the Walker circulation: Implications for projections. J. Climate, 28, 20–35, doi:10.1175/ JCLI-D-13-00752.1.

Tanelli, S., S. L. Durden, E. Im, K. S. Pak, D. G. Reinke, P. Partain, J. M. Haynes, and R. T. Marchand, 2008: CloudSat's Cloud Profiling Radar after two years in orbit: Performance, calibration, and processing. IEEE Trans. Geosci. Remote Sens., 46, 3560–3573, doi:10.1109/TGRS.2008.2002030.

Tobin, I., S. Bony, and R. Roca, 2012: Observational evidence for relationships between the degree of aggregation of deep convection, water vapor, surface fluxes, and radiation. J. Climate, 25, 6885–6904, https://doi.org/10.1175/JCLI-D-11-00258.1.

Trenberth, K. E., J. T. Fasullo, C. O'Dell, and T. Wong, 2010: Relationships between tropical sea surface temperature and top-of-atmosphere radiation. Geophys. Res. Lett., 37, L03702, doi:10.1029/ 2009GL042314.

Turk, F. J., and S. D. Miller, 2005: Toward improved characterization of remotely sensed precipitation regimes with MODIS/ AMSR-E blended data techniques. IEEE Trans. Geosci. Remote Sens., 43, 1059–1069.

Voigt, A., and T. A. Shaw, 2015: Circulation response to warming shaped by radiative changes of clouds and water vapour. Nat. Geosci., 8, 102–106, doi:10.1038/ngeo2345.

Waliser, D. E., R. Murtugudde, and L. Lucas, 2003: Indo-Pacific Ocean response to atmospheric intraseasonal variability. Part I: Austral summer and the Madden-Julian Oscillation. J. Geophys. Res., 108.3160, doi:10.1029/2002JC001620.

Wang, S., and A. H. Sobel, 2011: Response of convection to relative sea surface temperature: Cloud-resolving simulations in two and three dimensions. J. Geophys. Res., 116, D11119, doi:https://doi.org/10.1029/2010JD015347.

Wilcox, E. M., and V. Ramanathan, 2001: Scale dependence of the thermodynamic forcing of tropical monsoon clouds: Results from TRMM observations. J. Climate, 14, 1511–1524.

Wilheit, T., C. Kummerow, and R. Ferraro, 2003: Rainfall algorithms for AMSR-E. IEEE Trans. Geosci. Remote Sens., 41, 204–214.

Wood, R., 2012: Stratocumulus clouds. Mon. Wea. Rev., 140, 2373-2423, https://doi.org/10.1175/MWR-D-11-00121.1.

Xu, K.-M., T. Wong, B. A. Wielicki, L. Parker, and Z. A. Eitzen, 2005: Statistical analyses of satellite cloud object data from CERES. Part I: Methodology and preliminary results of 1998 El Niño/2000 La Niña. J. Climate, 18, 2497–2514, doi:https://doi.org/10.1175/JCLI3418.1.

Xu, K.-M., A. Cheng, and M. Zhang, 2010: Cloud-resolving simulation of low-cloud feedback to an increase in sea surface temperature. J. Atmos. Sci., 67, 730–748, doi:https://doi.org/10.1175/2009JAS3239.1.

Xu, K.-M., T. Wong, S. Dong, F. Chen, S. Kato, and P. C. Taylor, 2016a: Cloud object analysis of CERES Aqua observations of tropical and subtropical cloud regimes, Part I: Four-year climatology. J. Climate, 29, 1617–1638, doi:https://doi.org/10.1175/JCLI-D-14-00836.1.

Ying, J., and P. Huang, 2016: Cloud–radiation feedback as a leading source of uncertainty in the tropical Pacific SST warming pattern in CMIP5 models. J. Climate, 29, 3867–3881, doi:10.1175/JCLI-D-15-0796.1.

Zhang, M. H., R. D. Cess, and S. C. Xie, 1996: Relationship between cloud radiative forcing and sea surface temperatures over the entire tropical oceans. J. Climate, 9, 1374–1384, doi:10.1175/ 1520-0442(1996)009,1374: RBCRFA.2.0.CO;2.

Figures

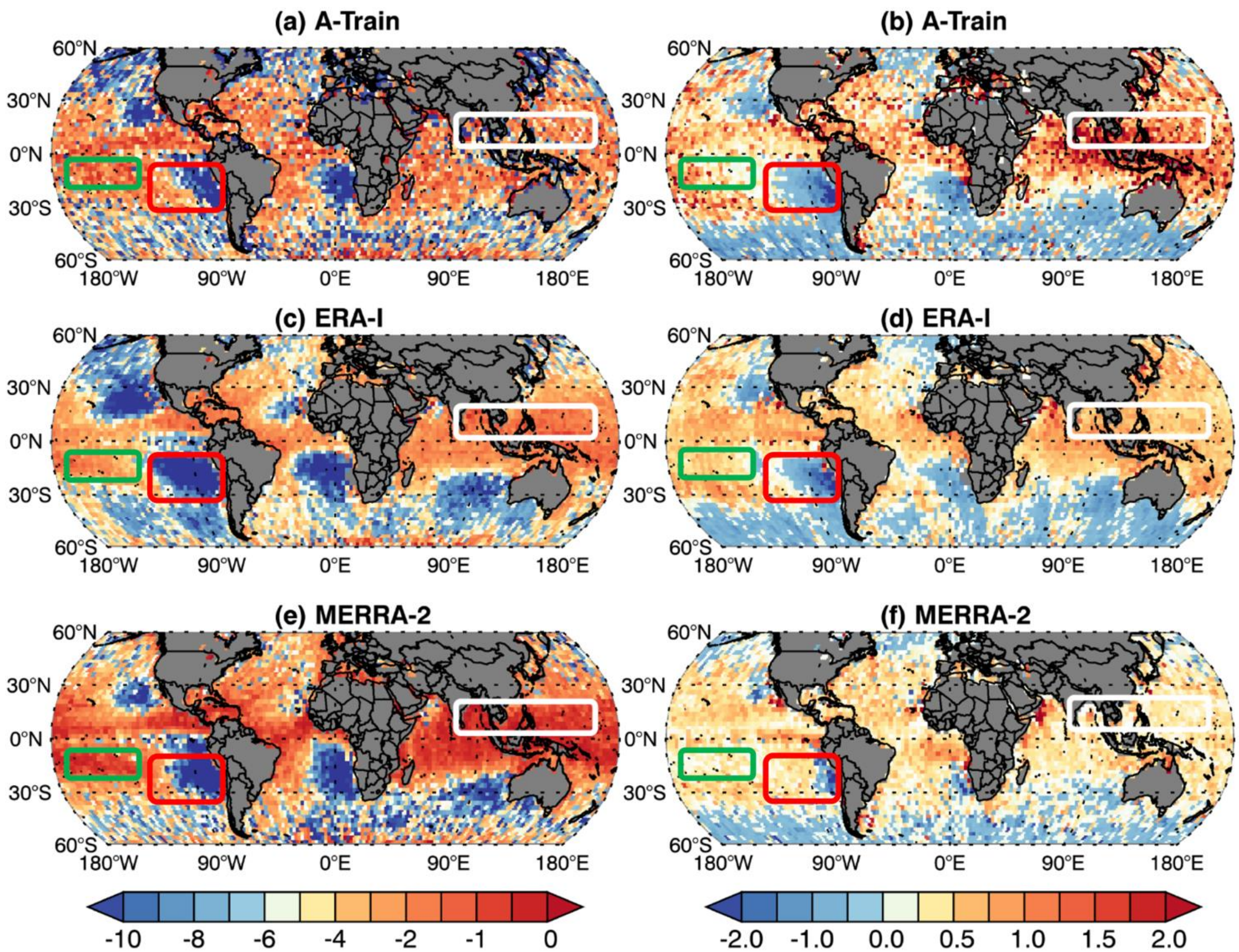

Figure 1: The global observed distributions of R_c (a, c, e) and R_h (b, d, e) derived from A-Train (a, b), ERA-Interim (c, d) and MERRA-2 (e, f) from September 2006 - December 2010.

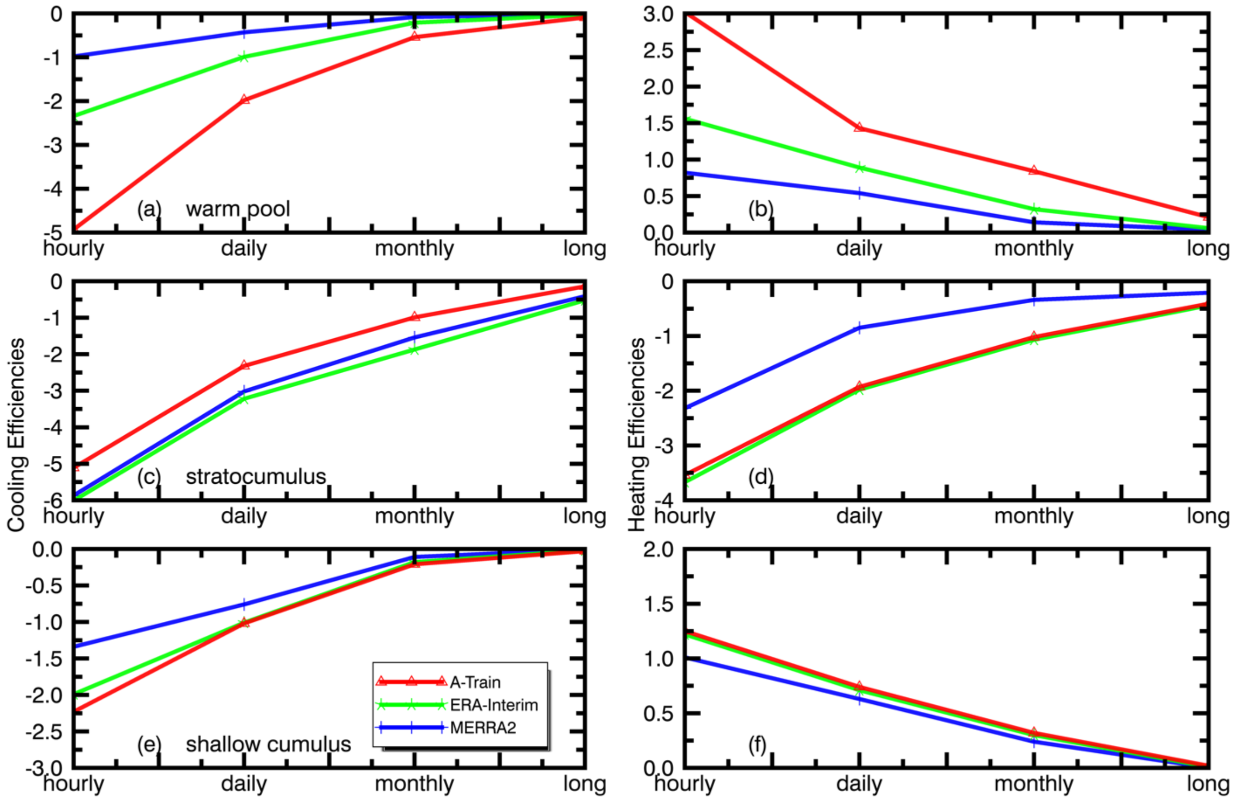

Figure 2: Time-scale dependence of both of R_c (left column) and R_h (right column) derived from A-Train, ERA-Interim, MERRA-2 for the three cloud regimes highlighted in Figure 1: (a, b) warm pool (25°S–15°N, 90–170°E), (c, d) stratocumulus (0–30°S, 70–100°W), and (e, f) shallow cumulus (15-30°S, 150–180°W).

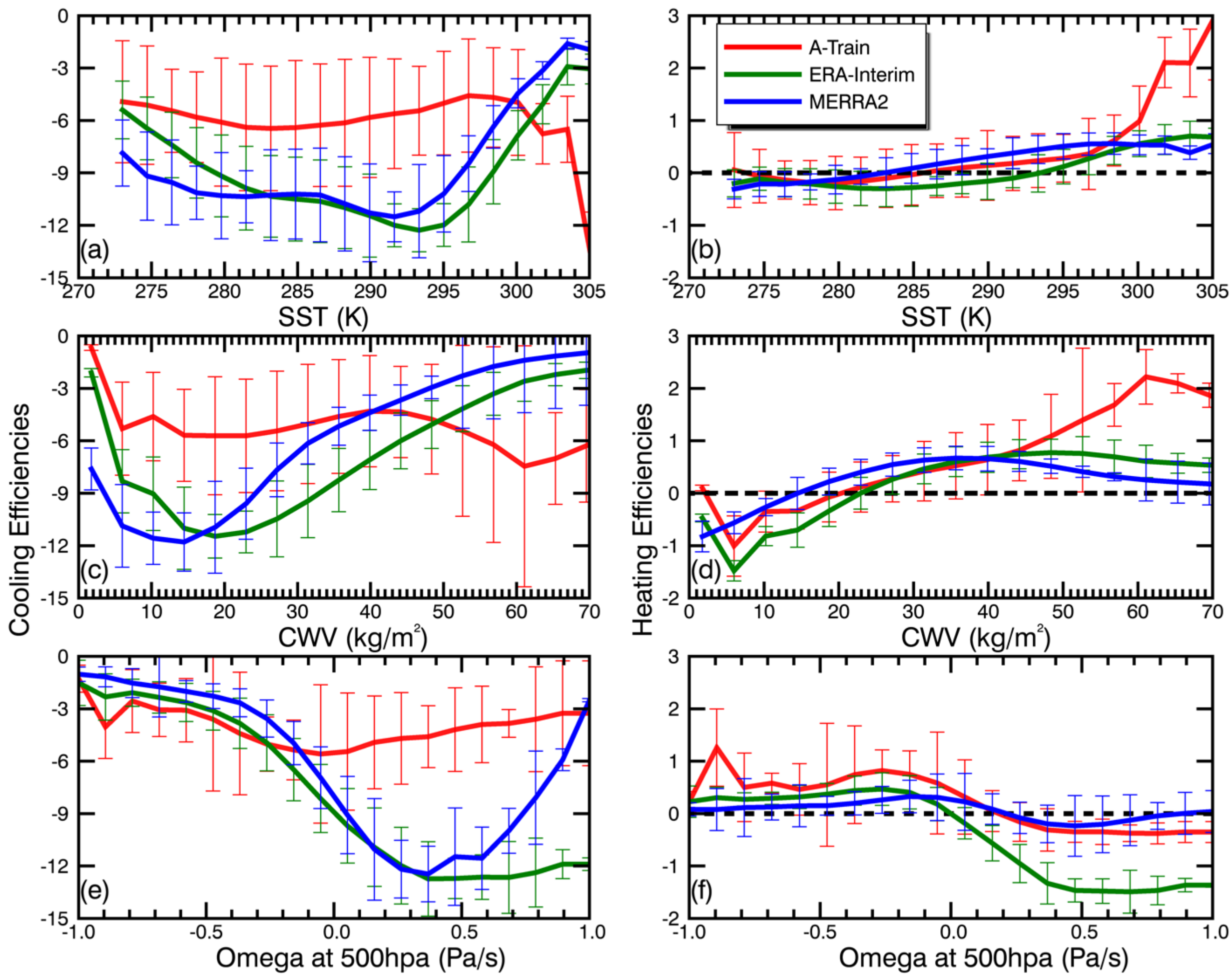

Figure 3: (a,c,e) R_c and (b,d,f) R_h as a function of (a,b) SST, (c,d) CWV, and (e,f) ω_{500}.

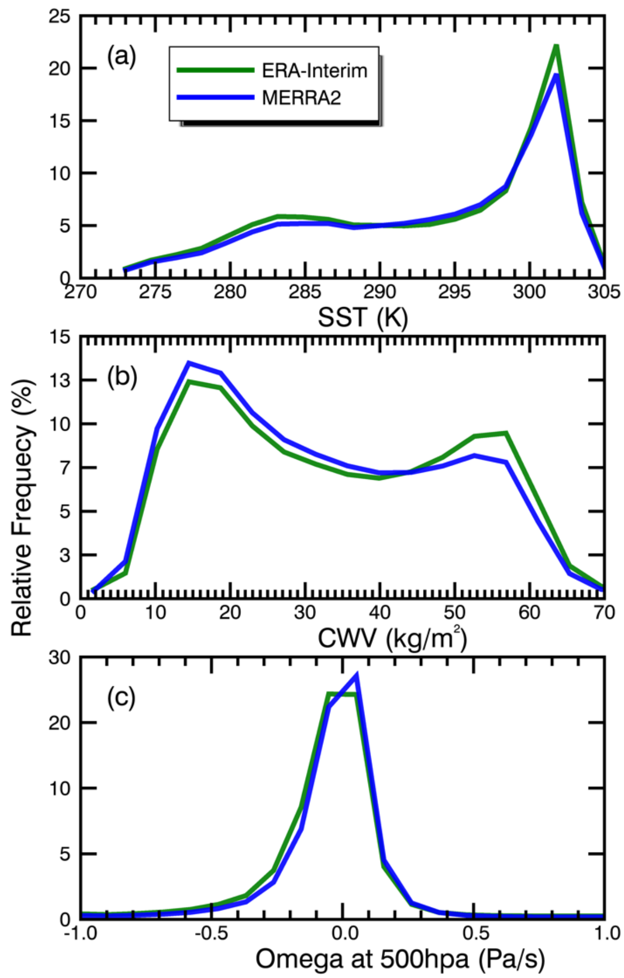

Figure 4: Distribution of the sample sizes at each bin corresponding to Figure 3. The blue line is the distribution of the sample sizes at each bin for MERRA-2 and the green line is A-Train and ERA-Interim. One should be noticed that A-Train and reanalysis have the same sample sizes as the ERA-Interim (green line) because all the R_c and R_h of A-Train have been matched with the environmental variables from ERA-Interim. R_c and R_h as a function of SST(a), CWV(b), and ω_{500}(c) obviously has the same sample size distributions.

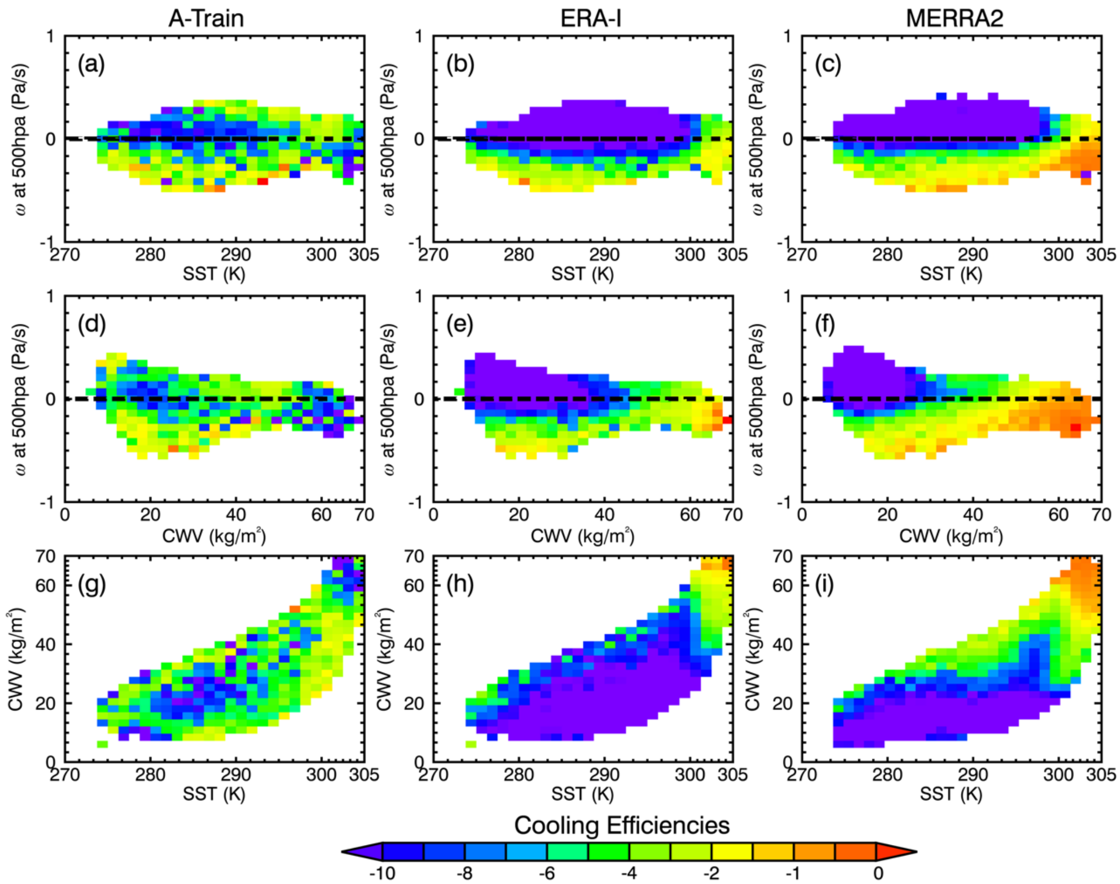

Figure 5: Joint distributions of mean R_c derived from A-Train/ERA-Interim/MERRA2 as a function of (a-c) SST vs. ω_{500}, (d-f) CWV vs. $\omega_{500,}$ (g-i) SST vs. CWV.

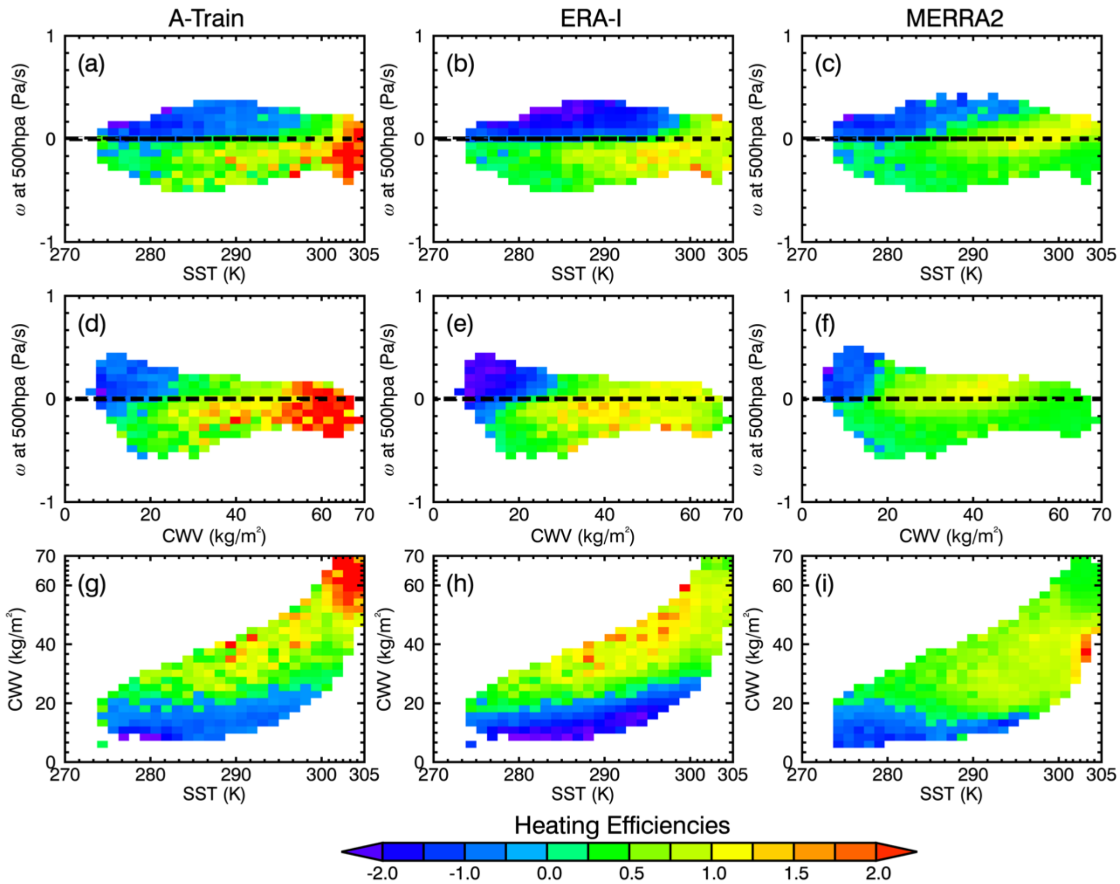

Figure 6: The same as Figure 5, but for $R_{h.}$

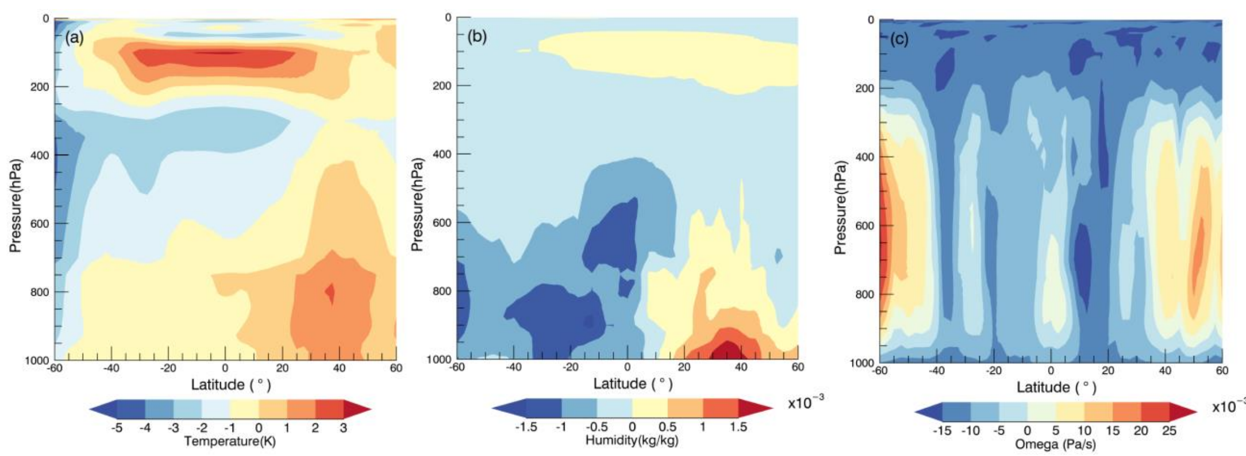

Figure 7: Zonal mean difference of the vertical profiles of (a) air temperature, (b) specific humidity, and (c) ω between ERA-Interim and MERRA-2 matching the A-Train samples between 2006-2010.